ORIGINAL ARTICLE

High-latitude mesospheric intense turbulence associated with high-speed solar wind streams

Young-Sook Lee[1] · Kyung-Chan Kim[2] · Young-Sil Kwak[3,4] · Yongha Kim[1]

Abstract Intense turbulence is frequently observed in the polar mesosphere summer echoes (PMSE) from the data of very high frequency radar operating at Esrange, Sweden. The turbulence can be estimated from the turbulent energy dissipation rate (ϵ) by considering aspect sensitivity. We find that variation in turbulence at altitude 82–86 km is in a good correlation with enhanced geomagnetic disturbances and precipitating energetic electrons into the mesosphere induced by high-speed solar wind streams. In addition, intense turbulence (a few tens of mW/kg) frequently occurs in the common volume with large plasma/neutral horizontal speeds (≥ 150 m s^{-1}) at 82–90 km altitudes. The large velocities are ready to form wind shear/shift. Therefore, we suggest that the summer mesospheric turbulence is to a significant extent accompanied by large plasma/neutral velocities and wind shear in the mesosphere, in turn linked to solar wind energy input during geomagnetic disturbances.

Keywords Turbulence · Polar summer mesosphere · Energetic electron precipitation · PMSE · Wind shear · Geomagnetic disturbances

✉ Y.-S. Lee
   mesoslight@gmail.com

1   Department of Astronomy and Space Science, Chungnam
    National University, Daejeon, Republic of Korea

2   Division of Science Education, College of Education, Daegu
    University, Gyeongsan, Republic of Korea

3   Korea Astronomy and Space Science Institute, Daejeon,
    Republic of Korea

4   Department of Astronomy and Space Science, University
    of Science and Technology, Daejeon, Republic of Korea

1 Introduction

The polar mesopause region exists in a unique thermal structure, reaching extremely low temperature less than 130 K in summer, colder than the radiative equilibrium, and in winter it turns to reach warm temperature of ∼190 K, warmer than the radiative equilibrium. This thermal structure is thought to be attributed to a pole-to-pole meridional circulation with adiabatic cooling (heating) due to ascent motion (subsidence) of air masses over from the summer to the winter poles. The meridional circulation is known to be driven by the momentum deposition of gravity wave breaking (Garcia 1989; Berger and von Zahn 1999).

In the upper mesosphere (80–90 km), turbulence is important as a dynamical heating source, comparable to other heating mechanisms including the absorption of solar UV and EUV radiation. Thus far, it has been understood that turbulence plays a role in transferring the potential and kinetic energy of upward propagating gravity waves to small spatial scales and converting this into heat by viscous dissipation (Smith et al. 1987; Fritts et al. 1988; Latteck et al. 2005). The turbulent energy dissipation rate in the mesosphere is typically in a range of 10–200 mW/kg, corresponding to heating rates of about 1–20 K/day. In the lower thermosphere of 100–120 km altitudes, turbulence can be enhanced by ion drag in the auroral region enforced by the electric field, which has been suggested by Hall and Aso (2000) as being mapped down from the magnetosphere. In the meanwhile, the link of mesospheric turbulence to solar wind-induced geomagnetic activity has been recently disclosed. In general, Polar Mesosphere Summer Echoes (PMSE) detectability is the result of the complicated effects of several factors including ice particles, turbulence and energetic electron precipitation during geomagnetic disturbances (Cho and Röttger 1997). Ice particle formation

initiated at ∼88 km in assumption goes through sediment and growth in radii as large as ∼20 nm (Rapp and Lübken 2004). The ice particle radii seemingly determine the lifetime of PMSE. Therefore, above ∼85 km PMSE with small radii last for a few minutes, and below ∼85 km with large radii resist for hours (Rapp et al. 2004). Above ∼85 km PMSE seem to exist as a result of large turbulence, and below this altitude iced particles are frozen in a plasma structure and last for a time, regardless of turbulence. Meanwhile, Rapp et al. (2004) observed large turbulence at 75–85 km altitudes as well as the larger one near 90 km altitude in summer by rocket experiments, for which an interpretation was given for the source coming from the upward propagating gravity waves (Fritts et al. 1988). Regardless, PMSE is also linked to high-energy particle precipitation as observed during high-speed solar wind streams (HSS) in solar minimum years (Gonzalez et al. 2006; Lee et al. 2013). Lee et al. (2014) found that PMSE and the turbulence are not completely controlled only by upward propagating gravity waves but also by energy input from solar wind interaction with the magnetosphere.

In this study, we examine whether intense turbulence occurring at 82–86 km altitudes would be associated with solar wind energy input during HSSs.

The paper consists of first deriving of turbulent energy dissipation rate in Sect. 2, second exploiting for intense turbulence how to be associated with solar wind energy input during HSS according to altitudinal divisions in PMSE layer (80–90 km) in Sect. 3, third investigating co-occurrence of intense turbulence with large echo speeds by presenting enlarged views of hour–to-hour variations of turbulent energy dissipation rate, reflectivity, and large echo speeds (> 150 ms^{-1}) in terms of time and altitude in section in Sect. 4, and fourth, investigating detailed wind patterns for selected cases of intense turbulence in Sect. 5. At last, discussion and, summary and conclusions are followed in Sects. 6 and 7, respectively.

2 Data and analysis

Turbulence energy dissipation rate is a tool of measuring turbulence. Turbulence can be observed from the radar with narrow beam width, since wide beam width antenna may have spectral broadening from non-turbulence sources, background winds including beam and/or shear broadenings, and gravity waves (Hocking 1983). Therefore, narrow beam is essential for reliable turbulence measurements using spectral widths to decrease the effect of non-turbulence broadening (Engler et al. 2005; Hocking 1983).

Esrange MST (Mesosphere-Staratosphere-Troposphere) radar (ESRAD) has a beam width of 5°, capably observing turbulent energy dissipation rate as long as radar sig-

nal strength is greater than 1 (Rapp et al. 2004). Spaced-antenna full correlation analysis (FCA) technique is employed for atmospheric wind velocity estimation of the Esrange MST radar (e.g., Briggs et al. 1950). The technique is based on spatio-temporal correlation of ground diffraction pattern resulting from the reflection of the volume scatterers (Holdsworth et al. 2001). The temporal properties are described by ground diffraction pattern lifetime, so called pattern lifetime ($T_{0.5}$). Turbulent energy dissipation rate is related to velocity fluctuation or turbulent random velocity. The random velocity of scattering irregularities is assumed as having an isotropic Gaussian distribution.

The turbulent velocity by means of FCA technique can be described with root-mean-square (RMS) random velocity related to pattern lifetime as in Eq. (1).

$$V_{fca} = \frac{\lambda\sqrt{2\ln 2}}{4\pi T_{0.5}}, \tag{1}$$

where λ is the wavelength of the radar and $T_{0.5}$ is the FCA pattern lifetime, an estimate of the correlation width in the frame of the ground diffraction pattern (Holdsworth et al. 2001).

A simplified formula can be given to estimate turbulent energy dissipation rate (ϵ) from the kinetic energy of the turbulence, related to V_{fca}^2, according to Hall et al. (1999) as in Eq. (2).

$$\epsilon = 0.8V_{fca}^2/T_B, \tag{2}$$

where T_B is the Brunt-Väisälä period. In the study, T_B is basically given as 5 min (the unit in sec) including uncertainties from $T_B = 3\text{–}6$ min (e.g., Hall et al. 2007; Wüst et al. 2017). Therefore, in this study turbulent velocity is an essential parameter in deriving turbulent energy dissipation rate.

Aspect sensitivity is considered in deriving turbulent velocity (Smirnova et al. 2012) and describes a property of the scatterer which may give various scattering power with respect to incident angle.

In the case of an isotropic scatterer, it is non-aspect sensitive. However, non-isotropic and specular scatterers suffer from aspect sensitivity. When scatterer radiates back the radiation transmitted from the radar, it can be described in a polar diagram defined by aspect sensitivity. Therefore, the backscatter pattern can be described by an effective polar diagram with the formula given by Hocking et al. (1986).

When every backscatter pattern (P) can be described in the polar diagram as in Eq. (3),

$$P(\theta) = \exp\left[-\frac{\sin^2\theta}{\sin^2\theta_0}\right], \tag{3}$$

where θ is zenith angle and θ_0 is e^{-1} half width of the polar diagram, the effective polar diagram can be composed with

polar diagrams of transmit and receive beams and that of the scatterers. The effective theta, θ_{eff} which is e^{-1} half width of the effective polar diagram can be given as Eq. (4),

$$\theta_{eff} = \frac{15.2\lambda\sqrt{R_{ax}}}{S_{0.5}}, \tag{4}$$

where λ is the radar wavelength, and $\sqrt{R_{ax}}$ and $S_{0.5}$ are the axis ratio and scale of the diffraction pattern, respectively (Holdsworth et al. 2001).

For the given e^{-1} half-widths of the radar transmit beam (θ_T) and of the radar receive beam (θ_R), the aspect sensitivity parameter θ_s can be derived from the equation:

$$\sin^{-2}\theta_s = \sin^{-2}\theta_{eff} - \left(\sin^{-2}\theta_T + \sin^{-2}\theta_R\right). \tag{5}$$

In this study, turbulence is estimated as long as $\theta_{eff} \geq 2.3$ or $\theta_s \geq 2.2$ if $\theta_{eff} < 2.3$. More details about the aspect sensitivity for ESRAD measurements can be found in Smirnova et al. (2012). The fca_150 mode is used to derive turbulent velocity, turbulent energy dissipation rate, and echo horizontal velocity, which is derived using FCA technique. In the mesosphere echo horizontal velocity is in primary a measure of plasma moving velocity, for which neutral velocity is treated as the same with that of plasma due to high neutral density. Reflectivity is derived from the fca_4500 mode data set. The altitude would be alternately expressed in range due to radar measurement in spite of the almost vertical view.

Geomagnetic field data at Esrange are obtained from Swedish Institute of Space Physics (http://www2.irf.se/). Solar wind parameters are obtained from OMNIWeb which is hosted by NASA (http://omniweb.gsfc.nasa.gov). Precipitating energetic electron fluxes (> 30 keV, > 100 keV) are derived from the observation of the Medium Energy Proton and Electron Detector (MEPED) instruments onboard Polar-orbiting Operational Environmental Satellites (POES) of NOAA-15, -16, and -18. The data is selected only when the NOAA/POES crosses over Esrange (0–40 °E and 64–72 °N).

3 Turbulence peak occurring in CIR region

Approaching solar minimum years, e.g., 2005–2008 in solar declining phase, HSS are a dominant source of driving geomagnetic disturbance, reaching a less intense Dst index than that by coronal mass ejection-driven storm (Tsurutani et al. 2006). Energetic electron (> 30 keV) precipitation lasts for 7, 9 or 13.5 day periods, having significant effects on F/E regions and D-region ionospheres, and on the thermosphere (Lei et al. 2008; Lee et al. 2013, 2014). HSS form a co-rotating interaction region (CIR) as it catches up with upstream slow solar wind. In the CIR, interplanetary magnetic field (IMF) and solar wind plasma are compressed to cause both intense fluctuation of the magnetic field and pressure pulse, respectively. The intense magnetic field fluctuation causes multiple magnetic reconnections and possible geomagnetic storms (or CIR-driven storms) (Smith and Wolfe 1976). The magnetic field, which is highly variable in the CIR, is usually associated with frequent southward turning of IMF Bz in the non-linear Alfvén waves (Tsurutani et al. 1995). The pressure pulse occurs as a result of the impingement of CIRs onto the magnetosphere, leading to direct injection of solar wind energy into the ionosphere (Craven et al. 1986). The solar wind energy transfer into the atmosphere is performed in the form of energetic electron precipitation and magnetic field pulsation. Pc5 pulsation is originally produced by solar wind dynamic pressure change (e.g., in CIR) and during the passage of HSS in the magnetosphere (Takahashi and Ukhorskiy 2007). The Pc5 wave in the magnetosphere modulates the chorus wave to cause pitch angle scattering of energetic electrons into the atmosphere, and produces, for example, pulsating aurora (Takahashi and Ukhorskiy 2007; Spanswick et al. 2005).

To trace the source of turbulence in PMSE, turbulent energy dissipation rate can be directly compared with solar wind and geomagnetic parameters in day-to-day variations, which are presented in Figs. 1a–1h, along with the relevant parameters. In a solar minimum year of 2006, the signature of recurrent HSS is clearly shown in the summer. Thus, marks of HSS1-HSS5 are assigned to each solar wind speed (V_{sw}) cycle in Fig. 1a. Before arrivals of HSS at the magnetopause, CIR formations (yellow, Figs. 1b–1c) are identified by proton density > 7 cm^{-3} (N_p), IMF magnitude > 3 nT (B_t) and a speed less than 450 m s^{-1} (Smith and Wolfe 1976; Tsurutani et al. 1995). In addition, CIRs are accompanied by fluctuations of IMF Bz and increases of AE (auroral electrojet) index as a proxy for geomagnetic activity (Figs. 1c–1d). In Figs. 1e–1f, turbulent energy dissipation rates (ϵ) are plotted for 86–90 km (blue) and 82–86 km altitudes (red), respectively. Here, lines (blue, red) are derived using $T_B = 5$ min and the shade is for uncertainties for $T_B = 3$–6 min. In a geomagnetically disturbed condition, e.g., AE$\geq$300 nT, at 82–86 km altitudes turbulent dissipation rate reaches up to $\epsilon > 18.0$ mW/kg, enhanced more than that ($\epsilon \cong 10.5$ mW/kg) of quiet time (i.e., AE < 100 nT) in hour-to-hour variation. Turbulent energy dissipation rates of 10–20 mW/kg are typical in the winter polar mesosphere around 90 km (Lubken 1997). And energy dissipation rates derived using VHF radar and rocket measurements in PMSE layer (about 80–90 km) were observed between 5–20 mW/kg at the lower edge and in the upper region of about 100 mW/kg (Engler et al. 2005). Therefore, turbulence becomes more intense with altitude, and thus in this study intense turbulence is defined with twice the average for each altitude region to be $\epsilon = 36$ mW/kg and 80 mW/kg in an hour resolution at 82–86 km and 86–90 km, respectively.

Fig. 1 PMSE-derived parameters including turbulent energy dissipation rate (mW/kg) and solar wind-related parameters in day-to-day variation for day from 150–190 (June 1–July 9), 2006. From the top, solar wind parameters of (**a**) solar wind speed (V_{sw}), (**b**) proton density (N_p), (**c**) interplanetary magnetic field (IMF) Bz and the magnitude (B_t, blue), and (**d**) AE index are shown in 1-min resolution (dark grey) and day-to-day variation (red); (**e**) turbulent energy dissipation rate (ϵ) for 86–90 km altitudes; (**f**) turbulent energy dissipation rate (ϵ) for 82–86 km, (**g**) PMSE occurrence, red for 82–86 km and blue for 86–90 km and (**h**) the reflectivity red for 82–86 km and blue for 86–90 km in day-to-day variations. The area filled in yellow indicates the CIR region
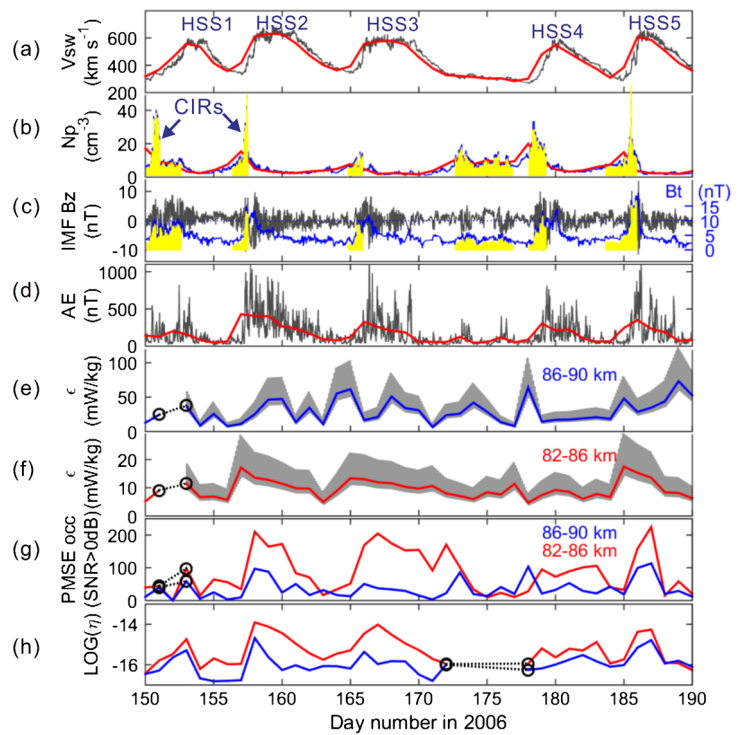
In Figs. 1g and 1h, PMSE occurrence and the reflectivity are also plotted for 82–86 km (red) and 86–90 km (blue), respectively. The average occurrence and reflectivity at 82–86 km altitudes become values of 94 and −15.4 (in 10-based log scale), much greater than those (40 and −16.1) at 86–90 km. At 82–86 km turbulence peaks precede PMSE peaks, implying that the turbulence possibly has an effect on PMSE increase. It is noticeable that at 82–86 km, turbulence peaks (contributed with intense turbulence) occur in most cases ahead of peaks of both AE index (red) and PMSE. However, above 86 km, turbulence seems not as effective on PMSE as at 82–86 km altitudes, or PMSE might be transient with short lifetime or rapidly sink down to the lower altitude (Rapp and Lübken 2003).To fully understand such tendency, scatter plots of the turbulent energy dissipation rate versus AE index are shown in Fig. 2 for different altitudes, (a) 82–86 km and (b) 86–90 km, respectively. It is clearly seen that turbulent energy dissipation rate at 82–86 km altitudes is well correlated with AE index. Large AE index can represent geomagnetic substorm to induce the enhancement of energetic electron precipitation, which can not only cause mesospheric neutral density increase but also Joule or/and particle heating in the mesosphere to induce intense turbulence accompanied by large ion/neutral velocity (Sinnhuber et al. 2012; Yi et al. 2017a, 2017b; Lee et al. 2018). Lee et al. (2018) observed large upward velocity is caused by enhanced energetic electron precipitation flux at the initiation of geomagnetic disturbance. The correlation is resulted in $R \approx 0.7$. However, above 86 km altitude, the turbulence, generally
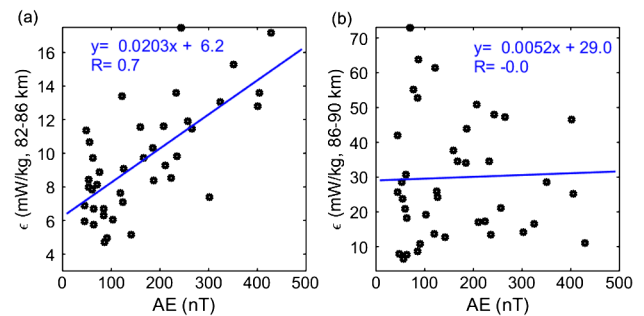

Fig. 2 Correlation between AE index and turbulent dissipation rate of altitude regions of (**a**) 82–86 km and (**b**) 86–90 km altitudes

more intense than that of 82–86 km altitudes, does not correspond well with the AE index.

4 Intense turbulence associated with large echo (plasma) speeds

Echo (plasma) horizontal speed exceeding 300 m s^{-1} derived by FCA technique from ESRAD measurements (Briggs 1984; Kirkwood et al. 2007) was named with echo extreme horizontal speed (EEHS) in Lee et al. (2014). The EEHS occurrence rate was enhanced by the effects of either CIR formation or HSS passage over the magnetosphere. In addition, peaks of EEHS occurrences are followed by PMSE of 7, 9 and 13.5 day periodicities in association with HSS emanating from coronal holes corotating with the Sun (Lee et al. 2013; Gonzalez et al. 2006).

Fig. 3 Enlarged views of turbulent energy dissipation rate responding to solar wind energy input for days = 156–162, 2006. (**a**) solar wind proton density (N_p) and the speed (V_{sw}), (**b**) IMF Bz, IMF magnitude (B_t) and dynamic pressure (P_{dyn}, against right axis), (**c**) Pc5 (1.6–6.7 mHz) H-component geomagnetic field measured at Kiruna, (**d**) POES-measured high-energy electron > 30 keV and > 100 keV precipitation flux, (**e**) turbulent energy dissipation rate (mW/kg) plotted in colored log scale in terms of time and range (1 hr and 1 km resolutions), (**f**) PMSE reflectivity and (**g**) turbulence extracted only if large horizontal plasma/neutral speeds ≥ 150 m s^{-1} within an hour; (**e**)–(**g**) Events A–E are noted for intense turbulence, for example, coexisting with large velocities
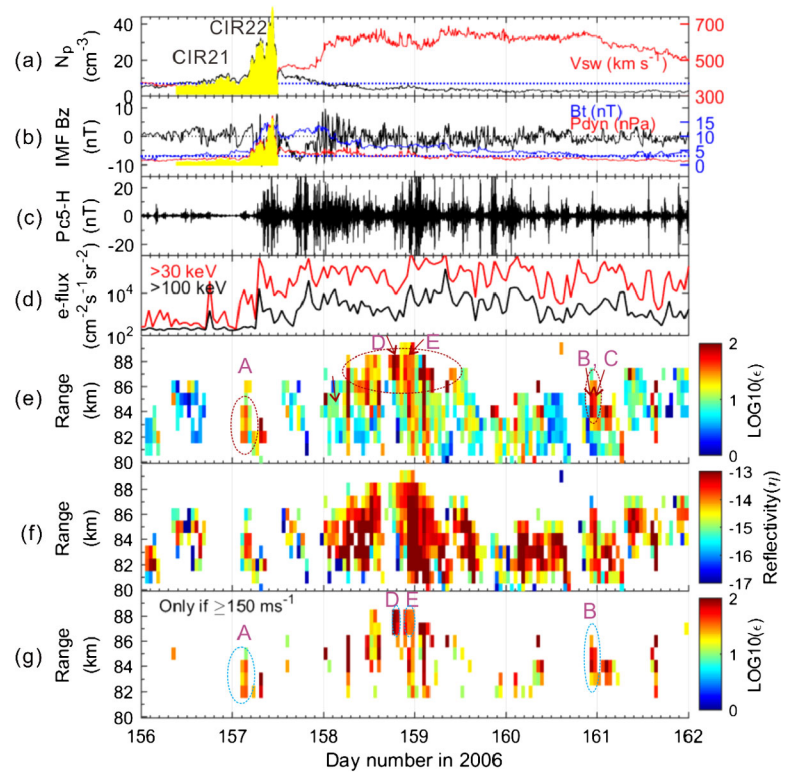

In the mesosphere, ion drift is affected only by electric field (E) but not by $E \times B$ drift (Heelis 2004), so that strong electric field can be a source of the fast-moving scatterers during the geomagnetic disturbance. Strong electric field was also suggested to explain the supersonic neutral speed that frequently accompanied the enhanced O(^{1}S) green line emission rates observed by The Wind Imaging Interferometer (WINDII) on board the Upper Atmosphere Research Satellite (UARS) (Lee and Shepherd 2010; Lee et al. 2016). The observations of supersonic neutral speed, most often occurring when polar mesospheric clouds (PMC) are present, were later complemented by EEHS observed in PMSE, suggesting that neutrals can be accelerated in a strong electric field by momentum transfer from the ions due to the high neutral-ion collision frequency (Heelis 2004). The acceleration of the neutrals by the large horizontal echo (plasma) speed in the mesosphere can consequently lead to wind shear, instability (e.g., Kelvin-Helmholtz instability) by the difference of flow velocities and high Reynolds number of turbulence (Fritts et al. 2016; Mann et al. 2016). As such, it is interesting to see how horizontal echo speeds are related to turbulent energy dissipation rate. In the upper mesosphere (80–90 km) echo horizontal speeds less than 150 m s^{-1} can be considered as the observation of neutral wind field (Liu et al. 2002). At the same time, echo speed ≥∼ 300 m s^{-1} actually exceeds the supersonic in the neutral speed at a low temperature less than 150 K (Lee and Shepherd 2010; Lee et al. 2016), so that

the subsonic becomes ∼ 240–300 m s^{-1}. Therefore, echo horizontal speed over 240 m s^{-1} can be assumed as a signature of localized acceleration by strong electric field and the accompanied speed over 150 m s^{-1} can also be taken into account on acceleration by the same source of strong electric field. Hereafter, large echo speeds over 150 m s^{-1} are applied for both ions and neutrals. PMSE was reported as well correlated with AE index, particularly when accompanied by HSS-induced geomagnetic disturbance (Lee et al. 2013). In the aspect, we examine the turbulence in detail in relation to CIR formation, as well as the duration of HSS passage over the magnetosphere ($V_{sw} \geq 450$ m s^{-1}) by selecting days 156–162 (HSS 2) in 2006.

Figure 3e shows turbulent energy dissipation rates with 1-hour and 1-km resolutions in terms of time and range for day number = 156–162, compared with the solar wind and geomagnetic parameters (Figs. 3a–3c) and energetic particle precipitation (Fig. 3d). In addition, PMSE reflectivity (Fig. 3f), and turbulence occurring with large speeds over 150 m s^{-1} (Fig. 3g) are also presented. The compression of HSS onto slower speed streams can be divided into two phases, for example, slow increase indicated with CIR21 as a leading part of CIR2 (day = 156.37–157.1) and fast increase indicated with CIR22 as a later part of CIR2 (until day = 157.43 (10:35 UT)) in terms of solar wind proton density (N_p), dynamic pressure (P_{dyn}) and IMF magnitude (B_t). For CIR21 an increasing rate of N_p is a value of 0.23 hPa/hr, while for CIR22 it is 4.2 hPa/hr to reach

Fig. 4 Same as in Fig. 3 except for day = 184–190, 2006
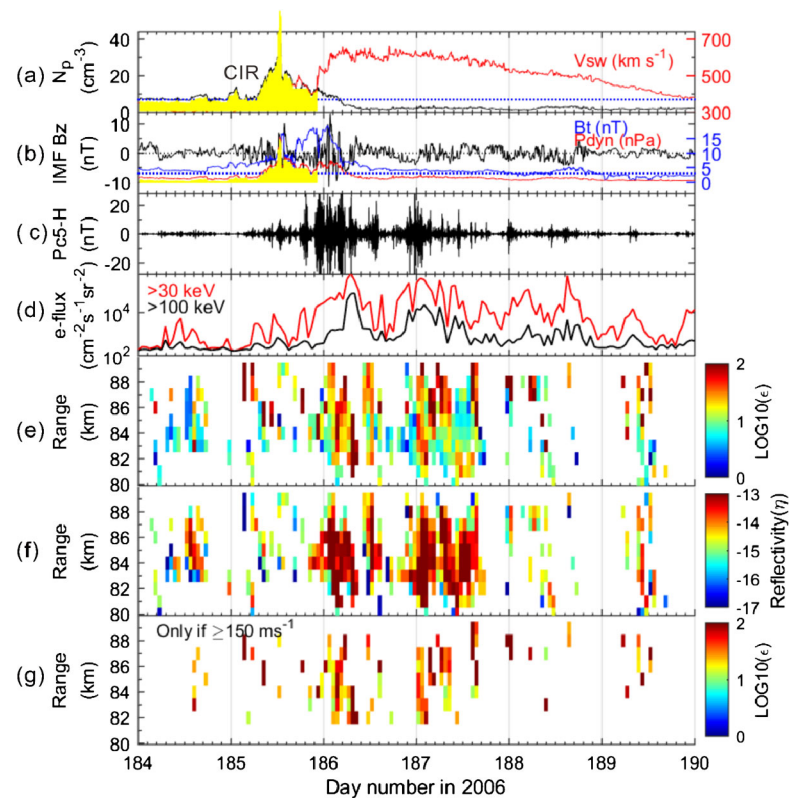

a peak from 157.1–157.5 (7–50 cm^{-3}). During both CIR phases, IMF Bz takes continual fluctuation with increasing magnitude. The estimated turbulence can be sourced from either the atmospheric turbulence or specular object (Smirnova et al. 2012). The turbulence, which is reflected from isotropic scatterers but not from specular scatterers, becomes ∼99% at 80–90 km by calculation, resolved in spatial and temporal grids of 1 km and 1 hr, respectively, as shown in Fig. 3e. Here, intense turbulence begins to occur near the initiation of CIR22, in which energetic electron flux is on increasing (Fig. 3d). Before 02:00 UT at day = 157 (∼157.1), PMSE were absent for about 10 hours with low Pc5 pulsation amplitude, although there was some energetic electron precipitation. However, after 02:00 UT, intense turbulence at most 36–41 mW/kg occurs between 02:00–04:00 UT (as indicated with A) (day = 157) at 82–86 km. This seems to be associated with an increase of high-energy electron precipitation and a slightly enhanced amplitude of Pc5-H component pulsations (Fig. 3c), in turn, linked to the formation of CIR. After event A, turbulence of PMSE is intensified from day number = 158.0 to the early day = 159 after some gaps and weak occurrences. Similarly, this pattern repeats such that during CIR creation intense turbulence appears for a short time, followed by a time gap and then continual intensification for 1–2 days while HSS pass over the magnetosphere. As shown in Fig. 3g, intense turbulence accompanied by echo speeds over 150 ms^{-1} as measured for an hour are extracted from those as shown in Fig. 3e.

Figure 4 shows another example of mesospheric turbulence and large velocities linked to the effects of CIR and HSS for days of 186 and 187. The CIR formation (yellow) and an increasing of solar wind speed induced by HSS are shortly followed by enhanced amplitudes of Pc5 oscillations of magnetometer H component and fluxes of energetic electron precipitation. Pc5 oscillations of magnetogram and energetic electron precipitation could fill the gap of the energy transfer from solar wind to the atmosphere. For PMSE at 82–86 km and 86–90 km the ratio of the speeds exceeding subsonic (≥ 240 ms^{-1}) to all the intense turbulence are values of 50.4% and 43.4%, and for speeds over 150 ms^{-1} are 80.7% and 75.0%, respectively. And the echo power (not shown) and reflectivity averaged over the selected intense turbulence as in Fig. 3f had values of 5.26 dB and -12.36 ± 1.04, respectively.

5 Case study of turbulence coexisting with large echo velocities

Turbulence can be linked to not only wave breakup, but also large echo (plasma) velocities, the wind shear and/or wind shift (e.g., Clark et al. 2000). In the mesosphere ion velocity is assumed as equalized with neutral velocity due to high neutral density. Increased turbulence related to the wind phenomena are demonstrated and discussed in this sec-

Fig. 5 Examples of wind shear/shift with large velocities to produce intense turbulence: (**a**) mVxVy and (**b**) mVyWz at 82–85 km altitudes for 2.6–3.4 UT on DOY = 157 (June 6, 2006); (**c**) mVxVy and (**d**) mVyWz at altitudes of 82–87 km for 22.0–23.5 UT on DOY = 160 (June 9, 2006); (**e**) mVxVy at 87–89 km altitudes for 18–20 UT, and (**f**) mVxWz at 87–89 km altitudes for 23–24 UT on DOY = 158 (June 7, 2006). Winds are colored in red for ≥ 240 m s^{-1} and in bright navy for 150–240 m s^{-1} in mVxVy (Figs. 5a, 5c, 5e). Winds are colored in orange for ≥ 50 m s^{-1} and in blue for < -50 m s^{-1} in mVyWz (Figs. 5b, 5d) and mVxWz (Fig. 5f). Here, vertical component of mWz is magnified 10 times greater than actual scale in order to make the vertical motion traceable. Events A ~ E are intense turbulences as shown in Fig. 3
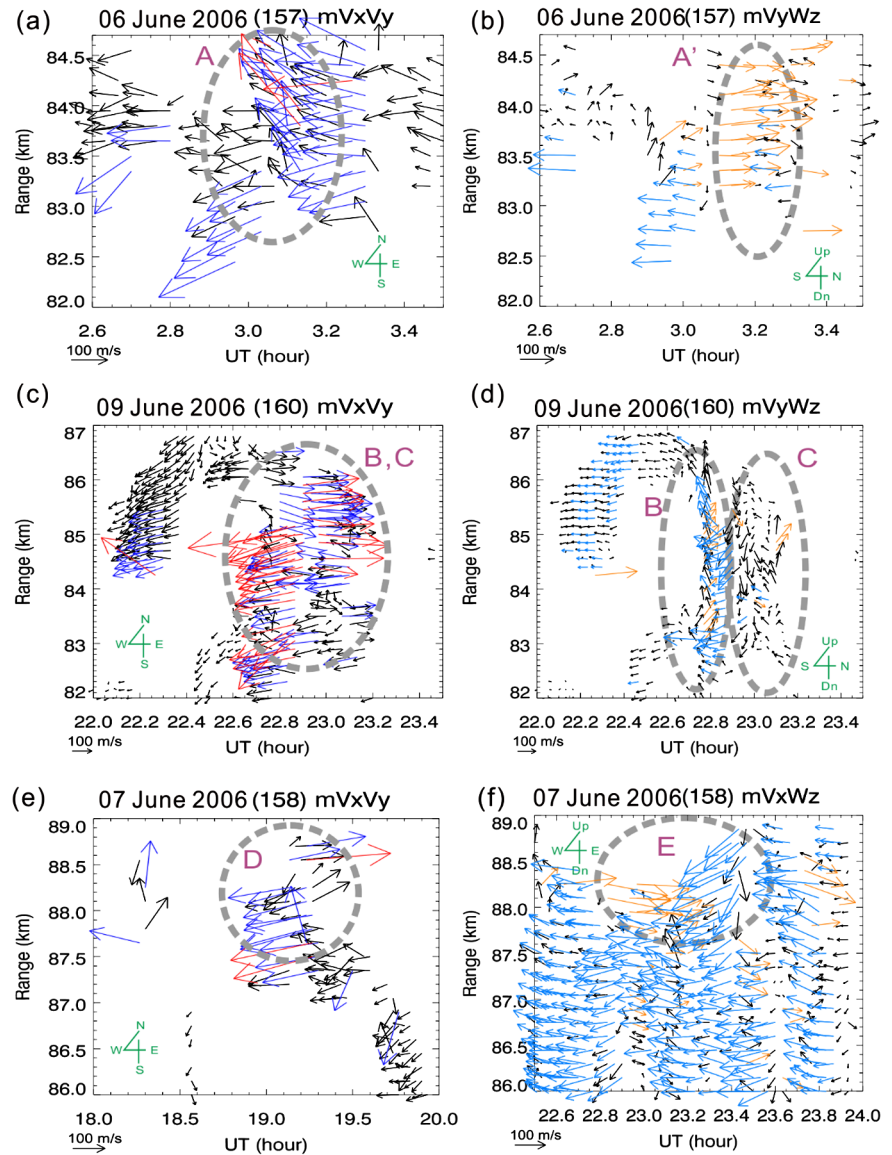
tion. Wind shear refers to a sharp change between horizontal wind speeds and/or the directions over different altitudes in a relatively short distance. When wind shear exists, the Kelvin–Helmholtz instability can occur, followed by vortex formation. Wind shift is defined as sudden change in wind direction more than 45° in less than 15 min with sustained wind speeds of 5 m s^{-1} in the troposphere. Wind shift occurs due to cold front, leading edge of cold air (Bluestein 1993).

In Figs. 5a–5f, wind shear and wind shift are, for example, presented in wind vector pairs of mVxVy, mVxWz or mVyWz, where mVx, mVy and mWz represent for zonal, meridional and vertical velocities in geomagnetic coordinates. The associated turbulent energy rates are estimated by using the method as in Sect. 2. Here, wind vector pairs are plotted in terms of time and range. Horizontal mVx and mVy wind vectors are represented according to magnetic coordinates. In the pair, for example, mVxVy, the first value,

mVx, is noted for the negative in leftward and for the positive in rightward, and the second one, mVy, is noted for the negative directing toward lower part and for the positive toward upper part. In each panel a pair of winds can be read as indicated with the four directional compass (green).

First, a bursting of large echo speeds is a candidate of producing intense turbulence, occurring for an hour. As shown in Fig. 5a, westward large echo speeds mVx ≤ -150 m s^{-1} including larger speeds ≤ -240 m s^{-1} (subsonic, supersonic, A) are concentrated on temporal and spatial regions of 02–04 UT (day = 157) and 82–86 km, in which westward winds are dominant. In the same circumstances, as shown in Fig. 5b, the large northward velocities (+mVy, 83.2–84.4 km) indicated with A' rapidly turn to the southward (−mVy) from ~ 100 m s^{-1} to less than −50 m s^{-1}. At 83–85 km, turbulence of event A has been enhanced to 38–41 mW/kg near 3.2 hr UT from 20–26 mW/kg before 03 UT

(in Fig. 3e). Here, the increased turbulence can be attributed to large westward velocities and wind shift from NW to SW.

Second, as shown in Figs. 5c–5d at ∼22.8 UT (day = 160), large echo speeds break out to the westward below ∼85 km and abruptly turning to the eastward above ∼85 km, leading to vertical shear as indicated with B, C. At the same time, meridional winds (mVy) in turn flip from southward to northward, and vice versa with altitudes as shown in Fig. 5d (B). Here, mVy makes more than three alternating vertical shears in an extension of ∼4 km just before 22.8 UT. At this moment, intense turbulence is derived, as values of 63–84 mW/kg at 84–85 km for B (Fig. 5c) and then of 48 mW/kg for C (Fig. 5d), as shown in Fig. 3e.

Third, at an early stage of HSS arrival recording at high speeds above 500 $km\,s^{-1}$, intense turbulence frequently tends to concentrate in the upper altitude region (86–89 km range, D, E) as shown in Fig. 3e and Figs. 5e–5f. We examine how the turbulence and wind pattern are associated when there is intense turbulence in the upper altitude region. As shown in Fig. 5e, as the wind shear of echo speeds (≥ 240 $m\,s^{-1}$) occurs, the corresponding turbulent energy dissipation rate becomes a value of 157.3 mW/kg at 88 km at 19.0–19.5 UT (D), day = 158 (Fig. 3e). In a few hours at ∼23 UT (in Fig. 5f), another wind shifts with slowly turning from ∼22.8 UT to 23.6 UT in ∼58 min (E) produce turbulence of $\epsilon = 58$ mW/kg (also in Fig. 3e). The turbulence induced from wind shifts at velocities of > 150 $m\,s^{-1}$ (E) in the zonal direction at ∼23 UT (E, Fig. 5f) is weaker than for the larger velocities and a vertical shear at ∼19.2 UT (D, Fig. 5e). As a result, large echo speeds induced-turbulence is mostly intense, as shown in Figs. 5a–5f. The large echo speeds are usually accompanied by shear and/or wind shift.

6 Discussion

During geomagnetic disturbance, the energy source of both large echo speeds and intense turbulence can be sourced from energetic electron precipitation scattered by chorus wave and ULF Pc5 pulsations. In addition, flux transfer events driven by the field reconnection between IMF and geomagnetic field are also a candidate for the large echo speed induced-intense turbulence in the mesosphere (e.g., Cerisier et al. 2005). Fast poleward moving ions at speeds of 500–2000 $m\,s^{-1}$ and large turbulence were observed by SuperDARN radar in the F-region ionosphere, and fast moving irregularities were observed in the measurements by HF, UHF, and VHF radars in the E-region ionosphere (Gorin et al. 2012). Since ion drift motion in the mesosphere/D-region ionosphere is controlled by an electric field (E), the large horizontal ion/neutral speed can be accelerated in a strong electric field induced by energetic electron precipitation and/or a flux transfer event during geomagnetically

disturbed condition (Lee et al. 2014). The mesospheric turbulence enhancement at geomagnetic disturbances can be supported by the observation that both vertical ion velocity enhancement and the following generation of gravity wave oscillation at the Buoyancy periods of 6 min, 8 min and then 20 min in transition were caused by enhanced geomagnetic activity induced by solar wind shock (Lee et al. 2018). Regarding the extreme horizontal echo speed reported by Lee et al. (2014), Sommer et al. (2016) argued the possibility that it was related to artefacts from a small number of discrete scatterers in the volume. However, intense turbulence at 82–86 km cannot be overlooked for noticeable effects of CIR and HSS-induced electron precipitation, in that both a significant correlation ($R = 0.7$) with AE index as shown in Fig. 1. Therefore, the intense turbulence possibly occurs in association with the large horizontal neutral speed, which is in turn linked to both frequent southward turning of IMF Bz and the proton density (or dynamic pressure) change in the CIRs as well as to the passage of HSS over the magnetosphere.

Turbulence is an important factor to contribute to FCA random velocity. As well, other factors can be considered including horizontal and vertical fluctuations of scatterer travel speed within the scattering volume (e.g. due to wind shears and gravity waves), temporal changes in echo strength from individual refractive-index irregularities and the triangle size effect (TSE), which leads to an overestimate of the random velocity for small antenna spacings (Holdsworth et al. 2001). The last of these, TSE, cannot explain increases in turbulence in particular geophysical conditions. Neutral wind shears and gravity waves also occur regardless of geomagnetic conditions. If they change during disturbed geomagnetic condition, it could present another issue for solar wind impact on the mesospheric dynamics. Therefore, fluctuations of the plasma travel speed within the volume due to electric field effects, or rapid changes in the echo strength of individual irregularities (for example, due to rapidly changing energetic particle precipitation) could indeed contribute more during disturbed geomagnetic conditions.

7 Summary and conclusions

This study observes polar mesospheric intense turbulence caused by geomagnetic disturbances induced by recurrent CIRs and HSS passage over the magnetosphere.

Turbulent energy dissipation rate and echo horizontal velocity are derived from Esrange MST radar with 5° zenith angle using FCA technique for day = 150–190, 2006, in which polar mesospheric summer echoes (PMSE) occur. Furthermore, turbulent energy dissipation rate is estimated to identify the variation of turbulence in relation to the variation of solar wind-induced geomagnetic activity.

The results are summarized as the following:

1. Turbulence at 82–86 km was found to have a correlation of $R \approx 0.7$ with AE index. Turbulence at 82–86 km becomes half that of 86–90 km in averages of 12.6 and 37.4 mW/kg, respectively, for day = 150–190.

2. It is noticeable that for the 82–86 km altitudes, turbulence peaks precede 1 day to PMSE peaks for each period of recurrent HSS, occurring by the effect of CIR formation.

3. The intense turbulence frequently occurs with large horizontal plasma/neutral velocity (≥ 150 m s^{-1}) including over 240 m s^{-1}, which are comparable to subsonic and supersonic neutral speeds. The large velocity was diagnosed as not originating from the atmospheric dynamics (e.g., breaking up of upward gravity wave) but from the ionization induced by the solar wind energy input into the atmosphere. Moreover, relativistic electron deposition from the magnetosphere into the stratosphere and mesosphere has been proposed as a driving source for atmospheric waves by increasing the temperature in a local atmospheric volume (Tsurutani et al. 2016).

The large horizontal velocity is apt to induce instability and turbulence in the mesosphere. Bursting of large velocities is frequently observed in the form of shear, and also generates intense turbulence as measured in hourly resolution. The results can bring up a serious doubt for the traditional understanding of intense mesospheric turbulence induced by the breaking of upward propagating gravity waves. In a disturbed geomagnetic condition, intense turbulence can also possibly be caused by short-lived irregularity as well as by large plasma velocity caused by rapidly changing energetic electron precipitation.

Publisher's Note Springer Nature remains neutral with regard to jurisdictional claims in published maps and institutional affiliations.

References

Berger, U., von Zahn, U.: The two-level structure of the mesopause: a model study. J. Geophys. Res. **104**, 22083–22093 (1999). https://doi.org/10.1029/1999JD900389

Bluestein, H.B.: Observations and Theory of Weather Systems. Vol. 2, Synoptic–Dynamic Meteorology in Midlatitudes p. 246. Oxford University Press, London (1993)

Briggs, B.H.: The analysis of spaced sensor records by correlation techniques. In: Handbook for MAP. SCOSTEP Secr., vol. 13, pp. 166–186. University of Illinois, Urbana (1984)

Briggs, B.H., Phillips, G.J., Shinn, D.H.: The analysis of observations on spaced receivers of the fading of radio signals. Proc. Phys. Soc. **63B**, 106–121 (1950)

Cerisier, J.-C., Marchaudon, A., Bosqued, J.-M., McWilliams, K., Frey, H.U., Bouhram, M., Laakso, H., Dunlop, M., Förster, M., Fazakerley, A.: Ionospheric signatures of plasma injections in the cusp triggered by solar wind pressure pulses. J. Geophys. Res. **110**, A08204 (2005). https://doi.org/10.1029/2004JA010962

Cho, J.Y.N., Röttger, J.: An updated review of polar mesosphere summer echoes: observation, theory, and their relationship to noctilucent clouds and subvisible aerosols. J. Geophys. Res. **102**, 2001–2020 (1997)

Clark, T.L., Hall William, D., Kerr, R.M., Middleton, D., Radke, L., et al.: Origins of aircraft-damaging clear-air turbulence during the 9 December 1992 Colorado downslope windstorm: numerical simulations and comparison with observations. J. Atmos. Sci. **57**, 1105–1131 (2000)

Craven, J.D., Frank, L.A., Russell, C.T., Smith, E.J., Lepping, R.P.: Global auroral responses to magnetospheric compressions by shocks in the solar wind: two case studies. In: Kamide, Y., Slavin, J.A. (eds.) Solar Wind-Magnetosphere Coupling, pp. 367–380. Terra Scientific Publishing Co., Tokyo (1986)

Engler, N., Latteck, R., Strelnikov, B., Singer, B., Rapp, M.: Turbulent energy dissipation rates observed by Doppler MST radar and by rocket-borne instruments during the MIDAS/MacWAVE campaign 2002. Ann. Geophys. **23**, 1147–1156 (2005)

Fritts, D.C., Smith, S.A., Ben Balsley, B., Philbrick, C.R.: Evidence of gravity wave saturation and local turbulence production in the summer mesosphere and lower thermosphere during the STATE experiment. J. Geophys. Res. **93**, 7015–7025 (1988)

Fritts, D.C., Wang, L., Geller, M.A., Lawrence, D.A., Werne, J., Balsley, B.B.: Numerical modeling of multiscale dynamics at a high Reynolds number: instabilities, turbulence, and an assessment of Ozmidov and Thorpe Scales. J. Atmos. Sci. **73**, 555–578 (2016)

Garcia, R.R.: Dynamics, radiation, and photochemistry in the mesosphere: implications for the formation of noctilucent clouds. J. Geophys. Res. **94**, 14,605–14,615 (1989)

Gonzalez, W.D., Guarnieri, F.L., Clua-Gonzalez, A.L., Echer, E., Alves, M.V., Ogino, T., Tsurutani, B.T.: Magnetospheric energetics during HILDCAAs. In: Recurrent Magnetic Storms: Corotating Solar Wind Streams. Geophys. Monogr. Ser., vol. 167, p. 175. Am. Geophys. Union, Washington (2006)

Gorin, J.D., Koustov, A.V., Makarevich, R.A., St.-Maurice, J.-P., Nozawa, S.: Velocity of E-region HF echoes under strongly-driven electrojet conditions. Ann. Geophys. **30**, 235–250 (2012)

Hall, C.M., Aso, T.: Identification of possible ion-drag induced neutral instability in the lower thermosphere over Svalbard. Earth Planets Space **52**, 639–643 (2000)

Hall, C.M., Hoppe, U.-P., Blix, T.A., Thrane, E.V., Manson, A.H., Meek, C.E.: Seasonal variation of turbulent energy dissipation rates in the polar mesosphere: a comparison of methods. Earth Planets Space **51**, 515–524 (1999)

Hall, C.M., Aso, T., Tsutsumi, M.: Atmospheric stability at 90 km, 78 °N, 16 °E. Earth Planets Space **59**, 157–164 (2007)

Heelis, R.: Electrodynamics in the low and middle latitude ionosphere: a tutorial. J. Atmos. Sol.-Terr. Phys. **66**, 825–838 (2004)

Hocking, W.K.: On the extraction of atmospheric turbulence parameters from radar backscatter Doppler spectra—I. Theory. J. Atmos. Terr. Phys. **45**(2/3), 89–102 (1983)

Hocking, W.K., Ruster, R., Czechowsky, P.: Absolute reflectivities and aspect sensitivities of VHF radio wave scatterers measured with the SOUSY radar. J. Atmos. Terr. Phys. **48**, 131–144 (1986)

Holdsworth, D.A., Vincent, R.A., Reid, I.M.: Mesospheric turbulent velocity estimation using the Buckland Park MF radar. Ann. Geophys. **19**, 1007–1017 (2001)

Kirkwood, S., Wolf, I., Nilsson, H., Dalin, P., Mikhaylova, D., Belova, E.: Polar mesosphere summer echoes at Wasa, Antarctica (73 °S): First observations and comparison with 68 °N. Geophys. Res. Lett. **34**, L15803 (2007). https://doi.org/10.1029/2007GL030516

Latteck, R., Singer, W., Hocking, W.H.: Measurement of turbulent kinetic energy dissipation rates in the mesosphere by a 3 MHz Doppler radar. Adv. Space Res. **35**, 1905–1910 (2005)

Lee, Y.-S., Shepherd, G.G.: Summer high-latitude mesospheric observations of supersonic bursts and O(^{1}S) emission rate with the UARS WINDII instrument and the association with sprites, meteors, and lightning. J. Geophys. Res. **115**, A00E26 (2010). https://doi.org/10.1029/2009JA014731

Lee, Y.-S., Kirkwood, S., Shepherd, G.G., Kwak, Y.-S., Kim, K.-C.: Long-periodic strong radar echoes in the summer polar D region correlated with oscillations of high-speed solar wind streams. Geophys. Res. Lett. **40**, 4160–4164 (2013). https://doi.org/10.1002/grl.50821

Lee, Y.-S., Kirkwood, S., Kwak, Y.-S., Kim, K.-C., Shepherd, G.G.: Polar summer mesospheric extreme horizontal drift speeds during interplanetary corotating interaction regions (CIRs) and high-speed solar wind streams: coupling between the solar wind and the mesosphere. J. Geophys. Res. Space Phys. **119**, 3883–3894 (2014). https://doi.org/10.1002/2014JA019790

Lee, Y.-S., Kwak, Y.-S., Kim, K.-C., Solheim, B., Lee, R., Lee, J.: Observation of atomic oxygen O(^{1}S) green-line speed solar wind streams. J. Geophys. Res. Space Phys. **121**, 1042–1054 (2016). https://doi.org/10.1002/2016JA023413

Lee, Y.-S., Kim, Y.H., Kim, K.-C., Kwak, Y.-S., Sergienko, T., Kirkwood, S., Johnsen, M.G.: EISCAT observation of wave-like fluctuations in vertical velocity of polar mesospheric summer echoes associated with a geomagnetic disturbance. J. Geophys. Res. Space Phys. **123**, 5182–5194 (2018). https://doi.org/10.1029/2018JA025399

Lei, J., Thayer, J.P., Forbes, J.M., Sutton, E.K., Nerem, R.S., et al.: Global thermospheric density variations caused by high-speed solar wind streams during the declining phase of solar cycle 23. J. Geophys. Res. **113**, A11303 (2008). https://doi.org/10.1029/2008JA013433

Liu, A., Hocking, W., Franke, S., Thayaparan, T.: Comparison of Na lidar and meteor radar wind measurements at Starfire Opical Range, NM, USA. J. Atmos. Sol.-Terr. Phys. **64**, 31–40 (2002)

Lubken, F.-J.: Seasonal variation of turbulent energy dissipation rates at high latitudes as determined by in situ measurements of neutral density fluctuations. J. Geophys. Res. **102**(D12), 13441–13456 (1997)

Mann, I., Häggström, I., Tjulin, A., Rostami, S., Anyairo, C.C., Dalin, P.: First wind shear observation in PMSE with the tristatic EISCAT VHF radar. J. Geophys. Res. Space Phys. **121**, 11,271–11,281 (2016). https://doi.org/10.1002/2016JA023080

Rapp, M., Lübken, F.-J.: On the nature of PMSE: electron diffusion in the vicinity of charged particles revisited. J. Geophys. Res. **108**(D8), 8437 (2003). https://doi.org/10.1029/2002JD002857

Rapp, M., Lübken, F.-J.: Polar mesosphere summer echoes (PMSE): review of observations and current understanding. Atmos. Chem. Phys. **4**, 2601–2633 (2004)

Rapp, M., Strelnikov, B., Müllemann, A., Lübken, F.-J., Fritts, D.C.: Turbulence measurements and implications for gravity wave dissipation during the MaCWAVE/MIDAS rocket program. Geophys. Res. Lett. **31**, L24S07 (2004). https://doi.org/10.1029/2003GL019325

Sinnhuber, M., Nieder, H., Wieters, N.: Energetic particle precipitation and the chemistry of the mesosphere/lower thermosphere. Surv. Geophys. **33**, 1281–1334 (2012)

Smirnova, M., Belova, E., Kirkwood, S.: Aspect sensitivity of polar mesosphere summer echoes based on ESRAD MST radar measurements in Kiruna, Sweden in 1997–2010. Ann. Geophys. **30**, 457–465 (2012)

Smith, E.J., Wolfe, J.H.: Observations of interaction regions and corotating shocks between one and five AU: Pioneers 10 and 11. Geophys. Res. Lett. **3**, 137–140 (1976). https://doi.org/10.1029/GL003i003p00137

Smith, S.A., Fritts, D.C., VanZandt, T.E.: Evidence for a saturated spectrum of atmospheric gravity waves. J. Atmos. Sci. **44**, 1404–1410 (1987)

Sommer, S., Chau, J.L., Schult, C.: On high time-range resolution observations of PMSE: statistical characteristics. J. Geophys. Res., Atmos. **121**, 6713–6722 (2016)

Spanswick, E., Donovan, E., Baker, G.: Pc5 modulation of high energy electron precipitation: particle interaction regions and scattering efficiency. Ann. Geophys. **23**, 1533–1542 (2005)

Takahashi, K., Ukhorskiy, A.Y.: Solar wind control of Pc5 pulsation power at geosynchronous orbit. J. Geophys. Res. **112**, A11205 (2007). https://doi.org/10.1029/2007JA012483

Tsurutani, B.T., Gonzalez, W.D., Gonzalez, A.L.C., Tang, F., Arballo, J.K., Okada, M.: Interplanetary origin of geomagnetic activity in the declining phase of the solar cycle. J. Geophys. Res. **100**(A11), 21717–21733 (1995). https://doi.org/10.1029/95JA01476

Tsurutani, B.T., Gonzalez, W.D., Gonzalez, A.L.C., Guarnieri, F.L., Gopalswamy, N., et al.: Corotating solar wind streams and recurrent geomagnetic activity: a review. J. Geophys. Res. **111**, A07S01 (2006). https://doi.org/10.1029/2005JA011273

Tsurutani, B.T., Hajra, R., Tanimori, T., Takada, A., Bhanu, R., Mannucci, A.J., Lakhina, G.S., et al.: Heliospheric plasma sheet (HPS) impingement onto the magnetosphere as a cause of relativistic electron dropouts (REDs) via coherent EMIC wave scattering with possible consequences for climate change mechanisms. J. Geophys. Res. Space Phys. **121**, 10,130–10,156 (2016). https://doi.org/10.1002/2016JA022499

Wüst, S., Bittner, M., Yee, J.-H., Mlynczak, M.G., Russell, J.M. III: Variability of the Brunt–Väisälä frequency at the OH* layer height. Atmos. Meas. Tech. **10**, 4895–4903 (2017)

Yi, W., Reid, I.M., Xue, X., Younger, J.P., Murphy, D.J., et al.: Response of neutral mesospheric density to geomagnetic forcing. Geophys. Res. Lett. **44**, 8647–8655 (2017a). https://doi.org/10.1002/2017GL074813

Yi, W., Reid, I.M., Xue, X., Younger, J.P., Spargo, A.J., et al.: First observation of mesosphere response to the solar wind high-speed streams. J. Geophys. Res. Space Phys. **122**, 9080–9088 (2017b). https://doi.org/10.1002/2017JA024446